

Molybdenum single-atom-bridged ReS₂–graphene heterostructures for boosting supercapacitor performance

Mahima Khandelwal, Ievgen Obraztsov, Aby Cheruvathoor Poullose, Shashank Sundriyal, Gabor Ersek, Oleg Usoltsev, Laura Simonelli, Giuseppe Portale, Radek Zbořil, Aristides Bakandritsos



PII: S1385-8947(25)06636-7

DOI: <https://doi.org/10.1016/j.cej.2025.165798>

Reference: CEJ 165798

To appear in:

Received date: 23 April 2025

Revised date: 26 June 2025

Accepted date: 7 July 2025

Please cite this article as: M. Khandelwal, I. Obraztsov, A.C. Poullose, et al., Molybdenum single-atom-bridged ReS₂–graphene heterostructures for boosting supercapacitor performance, (2024), <https://doi.org/10.1016/j.cej.2025.165798>

This is a PDF file of an article that has undergone enhancements after acceptance, such as the addition of a cover page and metadata, and formatting for readability, but it is not yet the definitive version of record. This version will undergo additional copyediting, typesetting and review before it is published in its final form, but we are providing this version to give early visibility of the article. Please note that, during the production process, errors may be discovered which could affect the content, and all legal disclaimers that apply to the journal pertain.

Molybdenum Single-Atom-Bridged ReS₂–Graphene Heterostructures for Boosting Supercapacitor Performance

Mahima Khandelwal^{1*}, Ievgen Obraztsov¹, Aby Cheruvathoor Poulouse¹, Shashank Sundriyal¹, Gabor Ersek², Oleg Usoltsev³, Laura Simonelli³, Giuseppe Portale², Radek Zbořil,^{1,4*} Aristides Bakandritsos^{1,4*}

¹Regional Center of Advanced Technologies and Materials, The Czech Advanced Technology and Research Institute (CATRIN), Palacký University Olomouc, Slechitellu 27, 779 00 Olomouc, Czech Republic

²Zernike Institute for Advanced Materials, University of Groningen, Nijemborg 3, 9747, Groningen, the Netherlands

³ALBA Synchrotron Light Facility, Carrer de la Llum 2-26, 08290, Cerdanyola del Vallès, Spain

⁴Nanotechnology Centre, Centre for Energy and Environmental Technologies, VSB–Technical University of Ostrava, 17. listopadu 2172/15, 708 00, Ostrava Poruba, Czech Republic

*Correspondence: mahima.khandelwal@upol.cz (Dr. Mahima Khandelwal); radek.zboril@upol.cz (Prof. Radek Zboril); a.bakandritsos@upol.cz (Dr. Aristides Bakandritsos)

Abstract

Rhenium disulfide (ReS₂), a two-dimensional transition metal dichalcogenide (TMD), possesses weak interlayer interactions and tunable band gap, however its limited charge storage and cycling stability hinder its application in supercapacitors (SCs). This work demonstrates a paradigm shift in the performance of ReS₂ by introducing molybdenum (Mo) single-atom reactive centers, leading to strong interfacial coupling with a nitrogen-doped graphene (GN3). Notably, Mo-nitrogen bonds are formed enhancing charge storage in the Mo-ReS₂@GN3 (MRG-2) heterostructure. The incorporation of Mo also induces p-type doping (beneficial for coupling with the n-type GN3), lowers the band gap, and enhances the activity of the in-plane sulfur

atoms. The MRG-2 electrode delivered 87% and 31% increase in capacitance compared to pristine ReS₂ and Mo-ReS₂, respectively, along with a four-fold enhancement in electrical conductivity. An asymmetric SC cell using MRG-2 as the negative and NiCo₂S₄/graphene as the positive electrode achieved exceptional gravimetric (54.3 Wh kg⁻¹ at 1.0 kW kg⁻¹), volumetric (110.5 mWh cm⁻³ at 0.940 W cm⁻³), and areal (54.3 μWh cm⁻² at 1.0 mW cm⁻²) energy densities, and remained stable for at least 10,000 cycles. These findings establish interfacial single-atom engineering as a transformative approach to optimizing TMD-based heterostructures for next-generation energy storage technologies.

Keywords: 2D transition metal dichalcogenides; single-atom engineering; interfacial coupling; N-doped graphene; supercapacitors

Introduction

Electrochemical energy storage has gained significant attention due to the increasing demand for sustainable and efficient energy solutions. Among various energy storage technologies, supercapacitors (SCs) stand out due to their rapid charge/discharge cycles, high power density, and exceptional longevity. However, their low gravimetric and volumetric energy density remains a significant challenge, limiting their applicability in energy-demanding applications.^[1,2] To address this issue, extensive research efforts have been directed toward the effective tuning of the physicochemical properties of structurally tailored materials, and on the efficient integration thereof, such as in electrodes based on graphene, transition metal dichalcogenides (TMDs), oxides or sulfides, MXenes, layered double hydroxides, covalent and

metal-organic frameworks (COFs and MOFs).^[3–12] The development of such materials is crucial not only for supercapacitors, but also in energy conversion processes, such as in water splitting, fuel cells, alcohol oxidation, and zinc-air batteries.^[13–16]

Two-dimensional (2D) TMDs have gained substantial attention in SC research, owing to their rich redox chemistry, unique layered structures, and 2D permeation channels that facilitate rapid ion diffusion.^[17–19] Among TMDs, MoS₂ can be stabilized in the conductive 1T phase and intercalate ions with extraordinary efficiency, delivering a volumetric energy density of 16 mWh cm⁻³ at a power density of 620 mW cm⁻³ in aqueous electrolytes.^[5] Quantum dots of MoS₂ rich in defects demonstrated 0.55 mWh cm⁻³ at 3 W cm⁻³.^[20] Oxygen-incorporation in the mixed 1T/2H MoS₂ phase and growth on graphite foil increased the interlayer spacing and conductivity, delivering a gravimetric energy density of 39.7 Wh kg⁻¹ at 450 W kg⁻¹.^[21] The usually decoupled interfaces between the inorganic electroactive species and their conductive counterparts (e.g., carbon black, graphene) is one of the bottlenecks in electrochemical processes.^[7,22] Therefore, heterostructures are developed with the aim to improve the charge transfer at the phase boundaries.^[22–25] MoS₂ grown on reduced graphene oxide (rGO), delivered 0.78 mWh cm⁻³,^[22] while the 1T/2H MoS₂ grown on pristine graphene reached 46.3 mWh cm⁻³.^[23] Moreover, the 1T-MoS₂ was grown on Ti₃C₂ to leverage the excellent conductivity of MXenes, which exhibited an areal energy density of 17.4 μWh cm⁻² at 0.6 mW cm⁻².^[24]

Rhenium disulfide (ReS₂) is a relatively newer member in the family of 2D TMD materials^[26] with unique properties, such as thermodynamically stable distorted 1T (1T') phase with inherent anisotropic structure leading to an extremely weak interlayer coupling (18 meV for ReS₂ vs. 460 meV for MoS₂) and large interlayer spacing.^[27] Moreover, the rich density of states of ReS₂ around the Fermi level shows that the band structure can be drastically modulated.^[28]

These characteristics enhance ion diffusion between layers, and facilitate access to electrochemically active sites.^[27,29] However, ReS₂ has a band gap of ca. 1.43 eV, leading to limited electronic conductivity, similar to other TMDs^[26,27] The electrochemical activity of the in-plane sulfur atoms is low due to their limited contribution to the density of states near the Fermi level, which is mainly populated by the orbitals of the edge sulfur atoms.^[30] Importantly, effective coupling between ReS₂ and conductive carbon counterparts has not yet been achieved, which is critical for fully exploiting the active material's electrochemical properties. As a result, so far, ReS₂ as a SC electrode material has demonstrated 25.3 Wh kg⁻¹ at 1.0 kW kg⁻¹, even in a high voltage organic electrolyte with 95.6% capacitance retention after 5,000 cycles.^[31] In aqueous electrolyte, 2D ReS₂ nanosheets embedded in a porous carbon framework delivered 4.2 Wh kg⁻¹ at 0.5 kW kg⁻¹, retaining 91.5% capacitance after 6,000 cycles.^[32] A symmetric SC based on a ReS₂/MoS₂ 2D heterostructure achieved an areal energy density of 1.94 μWh cm⁻² at 250 μW cm⁻², maintaining 66.5% capacitance after 10,000 cycles.^[33] Additionally, ReS₂ combined with conducting black phosphorous demonstrated 4.26 μWh cm⁻² but at lower power density of 41 μW cm⁻².^[34] Despite the intrinsic structural advantages of 2D 1T' ReS₂, its performance still lags behind leading systems in the field, as shown by recent literature (**Tables S1 and S2**).^[7,8,35] Fully realizing ReS₂'s electrochemical potential requires enhanced charge transfer, higher intrinsic activity, and strong interfacial coupling with a conductive counterpart.

On this basis, we sought to modulate the structure of 2D 1T' ReS₂ by incorporating molybdenum (Mo) single-atoms, which significantly enhance conductivity through pronounced band-gap reduction.^[28] Mo incorporation also boosts the contribution of the in-plane sulfur (S) atoms to the density of states around the Fermi level, rendering them as reactive as the edge S atoms in ReS₂.^[30] Moreover, Mo-ReS₂ is a p-type semiconductor, which is particularly beneficial

for strong interlayer coupling with n-doped systems,^[34,36] such as nitrogen-doped graphene. To exploit this synergy, a structurally and chemically tailored nitrogen-superdoped (16 at.%) graphene derivative (GN3)^[37] was strongly coupled with Mo single-atom engineered ReS₂ (Mo-ReS₂), affording for the first time a highly electrochemically active Mo-ReS₂@GN3 heterostructure. Extended X-ray absorption fine-structure spectroscopy (EXAFS) revealed the single-atom state of Mo and its remarkable coordination with the nitrogen (N) functionalities of GN3. The Mo-ReS₂@GN3 electrode demonstrated an 87% improvement in capacitance compared to pristine ReS₂ and a four-fold enhancement in conductivity. When integrated into an asymmetric SC (ASC), the device delivered an outstanding gravimetric (54.3 Wh kg⁻¹ at 1.0 kW kg⁻¹), and volumetric (110.5 mWh cm⁻³ at 0.940 W cm⁻³) energy density. The energy density was retained as high as 47.9 mWh cm⁻³ even at 37.7 W cm⁻³, with excellent long-term cycling stability (96.7% after 10,000 cycles). The areal density was also particularly high, reaching 54.3 μWh cm⁻² at 1.0 mW cm⁻². This Mo-ReS₂@GN3 based ASC outperformed not only previously reported ReS₂-based SCs, but also other 2D TMDs, as well as top-tier materials from the broader family of transition metal sulfides,^[7,8,38] and advanced SC electrode materials (**Tables S1 and S2**).^[6,9,10,39] This work introduces a previously unexplored approach, of Mo single-atom engineering in 1T' ReS₂ as a transformative strategy to mitigate the intrinsic limitations of low conductivity and electrochemical activity. Strong coupling with conductive, nitrogen-doped graphene fundamentally reshapes interfacial interactions and unlocks a previously unattainable level of charge-storage performance.

Results and Discussions

Mo single-atoms were successfully incorporated into the 2D ReS₂ network, and seamless coupling with GN3 was achieved through a facile hydrothermal route for 24 h at 240 °C (**Figure 1a**). The metal precursors used were ammonium perrhenate (NH₄ReO₄) and ammonium heptamolybdate ((NH₄)₆Mo₇O₂₄), while thiourea served as the sulfur source, enabling the formation of 2D Mo-ReS₂ nanosheets. Initially, three Mo-ReS₂ samples were synthesized (MR-1, MR-2, and MR-3) by varying the mass ratio(s) of NH₄ReO₄ to (NH₄)₆Mo₇O₂₄ (**Table S3**). Of the three, the optimally doped sample (Mo_{0.22}Re_{0.78}S₂; designated as MR-2), exhibited the highest capacitance and the lowest impedance (**Figure S1**; details discussed therein). This composition was obtained by using a precursor mass ratio of NH₄ReO₄ to (NH₄)₆Mo₇O₂₄ equal to 5.5 in the reaction (**Table S3**). This optimum ratio was employed for the in-situ growth of MR-2 in the presence of selectively and densely functionalized graphene derived via fluorographene chemistry i.e., highly conductive nitrogen-doped graphene (GN3). After testing three different GN3 loadings, the optimal Mo_{0.22}-Re_{0.78}S₂/GN3 ratio was identified according to capacitance and impedance measurements (**Figure S2**, sample name MRG-2). The MRG-2 heterostructure contained 9.2 wt.% GN3.

The X-ray diffraction (XRD) patterns of the synthesized pure 1T' ReS₂ (designated as PR), the Mo-doped system (MR-2), and the heterostructure with GN3 (MRG-2) exhibit main diffraction peaks at 14.3°, 32.5°, 43.7°, and 57.5°, corresponding to the (002), (-220), (210), and (-422) crystal planes, respectively, confirming the formation of 1T' ReS₂ (JCPDS 89-0341, **Figure 1b**).^[40,41] The XRD reflection at 14.3° corresponds to a *d*-spacing of 0.61 nm, attributed to the (002) crystal plane of PR. The same pattern was observed in MR-2 and MRG-2, confirming the crystal structure of ReS₂ after Mo doping and GN3 coupling, with no formation

of secondary phases or impurities. Wide-angle X-ray scattering (WAXS) measurements revealed a slight reduction of 0.10 Å in the interatomic distance of the (002) plane in MRG-2 compared with PR, as expected since Mo induces stronger interlayer interactions and makes exfoliation more difficult (**Figure S3**).^[27] The Raman spectrum of PR featured two characteristic peaks at 147.2 cm⁻¹ and 207.4 cm⁻¹ assigned to the in-plane (E_g) and out-of-plane (A_g) vibration modes of 1T' ReS₂ (**Figure 1c**).^[41–44] However, MR-2 showed slightly blue-shifted A_g and E_g vibrational modes by 2–3 cm⁻¹ due to p-type Mo doping in 1T' ReS₂, attributed to electron-phonon coupling in TMDs.^[44,45] The p-type Mo doping in ReS₂ enhances hole carrier density, enabling interaction with incoming photons and causing a Raman shift toward higher frequencies, as similarly observed in chemical vapor deposited Mo-doped ReS₂ films^[44] (**Figure 1c**). Similar Raman shifts were also observed in MRG-2, along with the presence of D and G bands from GN3 (**Figure S4**). The G band in MRG-2 was redshifted by 7 cm⁻¹ compared to GN3, indicating strong electronic interactions and charge transfer from N atoms of GN3 to Mo-doped ReS₂ (**Figure S4**), similar to observations in graphene quantum dots acting as charge transfer bridge in MoSe₂ heterostructures.^[46] The Fourier transform infrared (FTIR) spectroscopy (**Figure S5**) exhibited bands at 1110 and 1417 cm⁻¹ corresponding to Re-S bonds^[47] in MR-2, which shifted to lower energy vibrations (1082 and 1402 cm⁻¹ in MRG-2), indicating a weakening of the Re-S bonds due to the changes in the coordination environment. Additionally, a new band appeared in MRG-2 at around 1560 cm⁻¹ (C=C, sp²),^[37] corresponding to the aromatic carbons in GN3. The small-angle X-ray scattering (SAXS) measurements demonstrated increased scattering in the low-q region of MRG-2 compared to PR, suggesting the development of a more hierarchical and interconnected porous network in the MRG-2 heterostructure (**Figure 1d**).

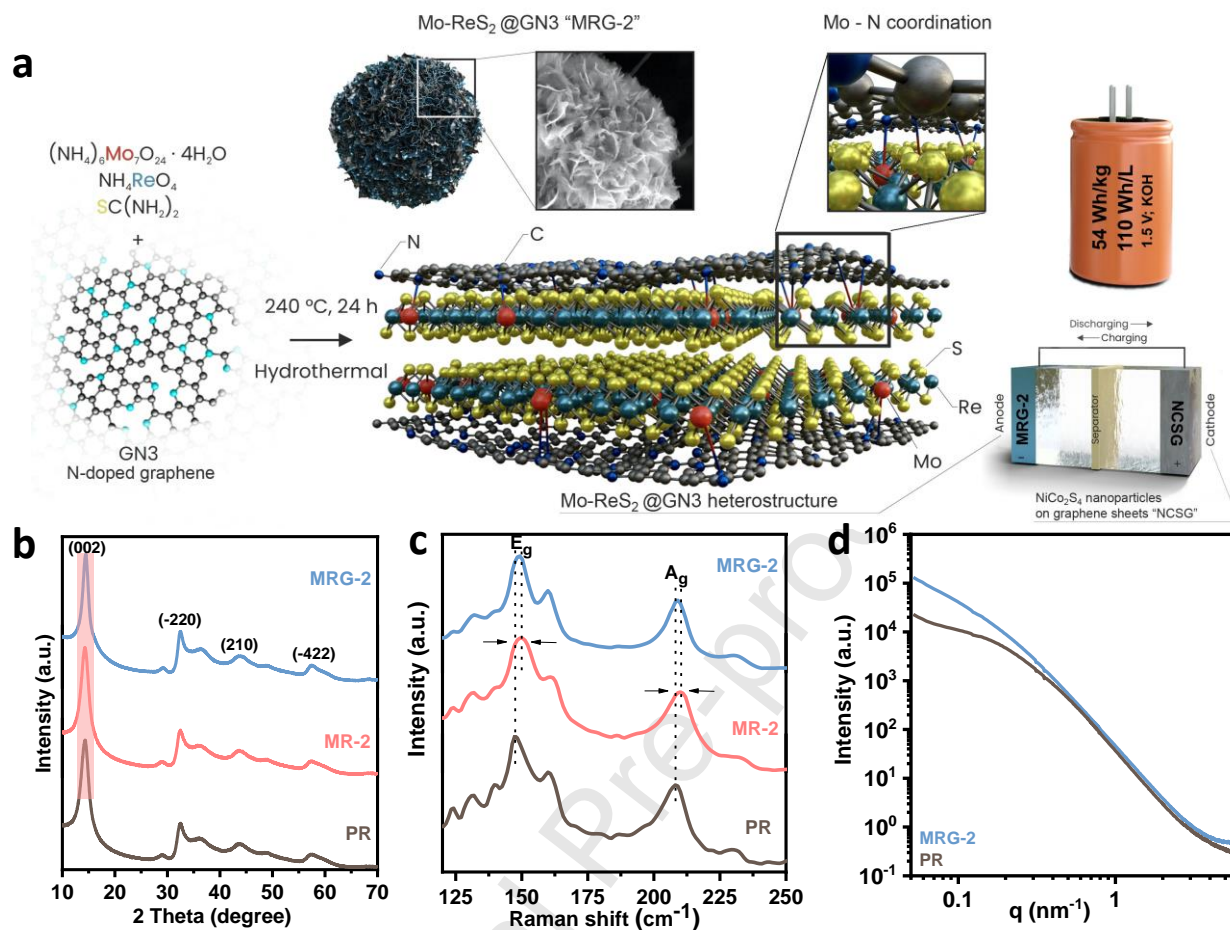


Figure 1. (a) Schematic illustration of the synthesis of MRG-2 showing the Mo single metal atoms incorporated into the ReS₂ sheets, and their covalent interactions with N atoms in GN3. The Mo-N coordination illustrated here is confirmed by EXAFS analysis (*vide infra*). The energy density values of the supercapacitor are based on the electrochemical results discussed later (see Figure 6). (b) XRD and (c) Raman measurements of PR, MR-2, and MRG-2. (d) SAXS measurements of PR and MRG-2.

The scanning electron microscopy (SEM) image of PR revealed the formation of 2D nanosheets assembled into flower-like arrangement (**Figure 2a**). The sheet-like morphology of PR remained intact after the incorporation of Mo single metal atoms and seamless coupling with GN3 (**Figure 2b, c**). Transmission electron microscopy (TEM) of PR also showed nanosheets

with a d -spacing of 0.61 nm (as in XRD) (**Figure 2d**). TEM and high-resolution TEM (HRTEM) images of MRG-2 (**Figure 2e, f**) reveal that the nanosheets are intimately mixed with the GN3 matrix, consisting of few layers (4-8 layers, **Figure 2f, g**), while the PR and MR-2 samples appear to consist of thicker bundles (4-12 layers) (**Figures 2d and S6**). The ReS_2 layers appear more densely packed (**Figure 2d**) in PR and MR-2, than in GN3-coupled MRG-2 sample (**Figure 2f**), corroborating with the SAXS results for an improved hierarchical and porous network (**Figure 1d**). The reduced number of ReS_2 layers in MRG-2, compared to PR and MR-2, is attributed to the high surface area and to the 2D conductive scaffold of GN3. GN3 is coupled with the Mo atoms in the MRG-2 material, weakening the interlayer interactions between the Mo- ReS_2 sheets, and promoting the formation of a less dense architecture. This sparser arrangement in MRG-2 increases the electrochemically accessible surface area, providing more active sites for sorption of ions, facilitating the efficient transport of electrolyte ions within the electrode material. The HRTEM image of MRG-2 shows amorphous GN3 layers at the edges and a crystalline structure with lattice d -spacings of 0.60 nm and 0.28 nm (**Figure 2g and inset**), corresponding to the (002) and (-220) $1\text{T}'$ ReS_2 planes, respectively. The d -spacing corresponding to the (002) was reduced by 0.10 Å in MRG-2 compared with PR, corroborating well with the WAXS results (**Figure S3**). High-angle annular dark-field HRTEM (HAADF-HRTEM) elemental mapping of MRG-2 revealed the homogeneous distribution of molybdenum over rhenium and sulfur from ReS_2 , along with the presence of carbon and nitrogen (originating from GN3), demonstrating the intimate and interwoven Mo- ReS_2 /GN3 coupling (**Figure 2h-m**). The Mo- ReS_2 in the MRG-2 sample retained the morphological structure of the parent $1\text{T}'$ ReS_2 , yet displayed an enhanced Brunauer-Emmett-Teller (BET) surface area of MRG-2 by ~ 1.5 times compared with PR (**Figure S7a, b**). This is attributed to GN3 incorporation acting as a high-

affinity dilution matrix for ReS_2 , yielding a larger porous network and enhanced surface area. The adsorption-desorption isotherms of MRG-2 showed a typical type-IV isotherm with a hysteresis loop in the relative pressure range of 0.4 –1.00, indicating its mesoporous nature.^[48] The total pore diameter of MRG-2 increased significantly to 32.1 nm, compared to PR's 5.9 nm (**Figure S7c, d**). This remarkable enhancement indicates that the use of GN3 as a template for the growth of 2D Mo-ReS_2 facilitated the formation of an expanded, interconnected pore network with multilevel pores in the hybrid structure. These findings align with the SAXS measurements (**Figure 1d**) and reveal an advantageous architecture for efficient electrolyte ion transport.

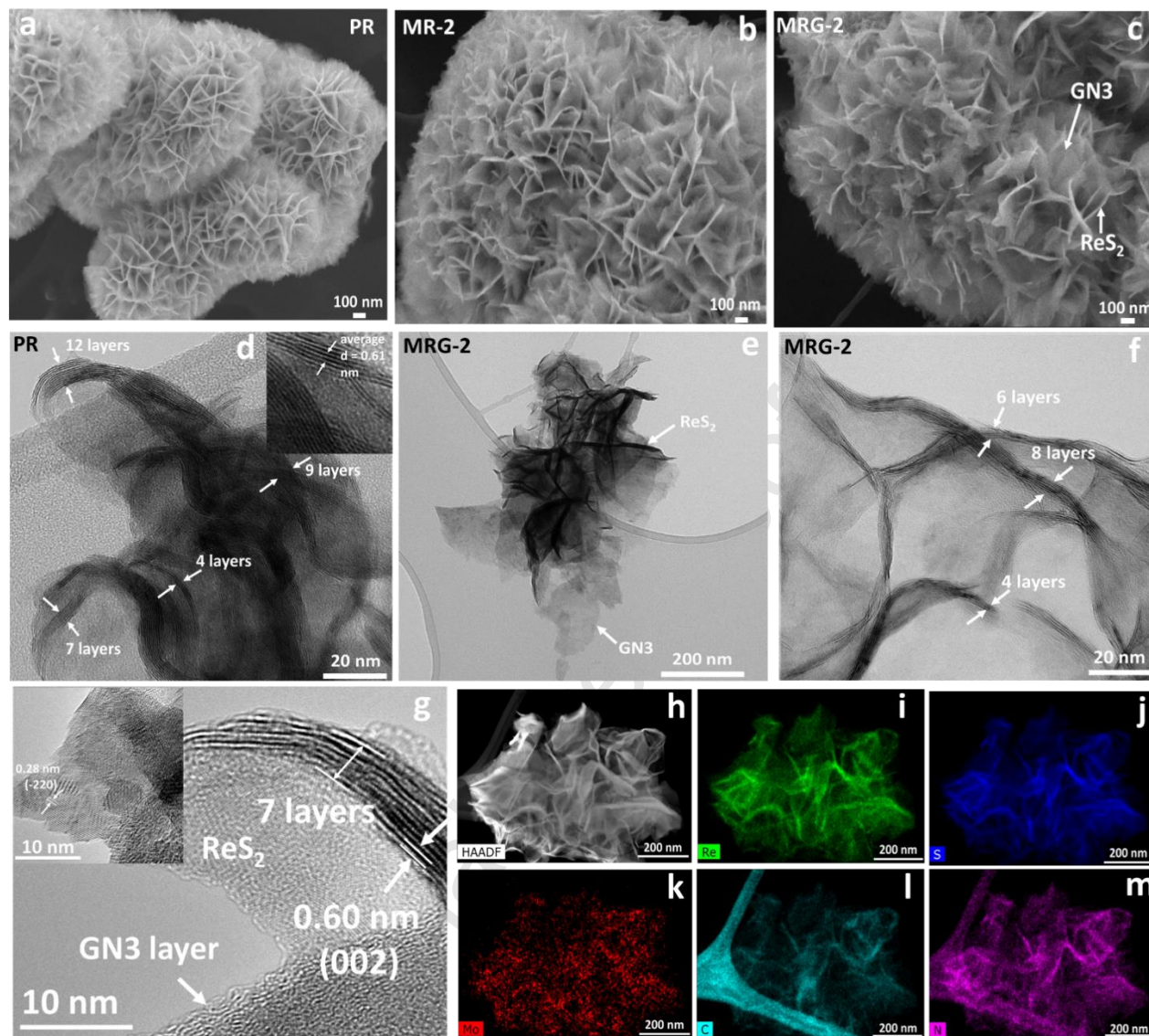


Figure 2. (a) SEM images of PR, (b) MRG-2, and (c) MRG-2. (d) HRTEM image of PR, (e-g) TEM and HRTEM images of MRG-2. (h) HAADF-HRTEM image of MRG-2 and the corresponding elemental mapping images for (i) rhenium, (j) sulfur, (k) molybdenum, (l) carbon, and (m) nitrogen.

X-ray photoelectron spectroscopy (XPS) revealed that the surface composition of MRG-2 is 26.2 at.% Re, 54.1 at.% S, 16.7 at.% C, and 1.5 at.% N. Because the Mo 3p and S 2s peaks have similar binding energies, accurate Mo quantification by XPS is difficult; thus, we determined the Mo content by ICP-MS (8.3 wt.%). The Re 4f spectrum of PR is deconvoluted

into two core components at 44.6 eV (Re 4f_{7/2}) and 42.2 eV (Re 4f_{5/2}) (**Figure 3a**) suggesting Re in the form of Re⁴⁺, while the S 2p spectrum shows components at 164.0 eV (S2p_{1/2}) and 162.7 eV (S2p_{3/2}), indicating S²⁻ (**Figure 3b**).^[40,43] These results confirm the formation of 1T' ReS₂.^[40,42,43] After incorporating Mo single-atoms and coupling with GN3, the characteristic bands corresponding to the formation of PR did not change significantly, except for a shift in the binding energies of Re 4f and S 2p to lower values (**Figure 3a, b**). This shift in MR-2 and MRG-2 is attributed to the lowering of the Fermi level to the valence band (thus, increased electron density of the Re and S orbitals which contribute to the valence band) due to p-type Mo doping, as similarly observed in previous studies on Mo-ReS₂ and on other p-type doped TMDs.^[44,49,50] The band gap reduction in p-type doped Mo-ReS₂ (theoretically^[28] and experimentally verified, **Figure S8**) allows easier excitation of charge carriers, increasing hole mobility within the valence band, and enables faster charge transport in the electrode material (as later discussed). The deconvoluted Mo 3d spectrum of MR-2 shows Mo 3d_{5/2} (228.9 eV) and 3d_{3/2} (232.0 eV) bands, corresponding to Mo⁴⁺ (**Figure 3c**).^[42,51] The Mo bands marginally shifted toward higher binding energy by ~0.2 eV after coupling with GN3, likely due to the electron transfer from Mo to the strongly electronegative N atoms of GN3 (**Figure 3c**), although the Mo statistics in MRG-2 do not allow for a conclusive statement.^[52] The direct interaction of the Mo atoms with N is later discussed in the extended EXAFS results. The N 1s deconvoluted spectrum of MRG-2 showed components approximately at 398.2 eV (pyridinic-N), 399.7 eV (pyrrolic-N), and 401.4 eV (graphitic-N). However, the nitrogen signal in MRG-2 was poor because of the low content of GN3 in the heterostructure, and thus of N (1.5 at.%, **Figure 3d**). In the N 1s high resolution XPS of the MRG-2 sample, a new component at 394.8 eV emerged, which is assigned to Mo 3p_{3/2}.^[53]

To better understand the coordination environment of Mo in the MRG-2 sample Mo K-edge X-ray absorption spectroscopy was performed. The Mo K-edge absorption near edge structure (XANES) signal in MRG-2 was similar to the MoS₂ reference sample (**Figure 3e**), but showing broadened features, compatibly to the coexistence of an additional Mo minority phase. The near-edge absorption energy for MRG-2 matches MoS₂ in the Mo K-edge XANES spectra, indicating a Mo⁴⁺ state, in agreement with XPS (**Figure 3c**). The corresponding k^3 -weighted EXAFS oscillations of MRG-2 are strongly damped relative to MoS₂ reference sample, suggesting higher local disorder; the low signal at high k values further indicates the absence of Mo-Mo bonds (**Figure 3f**). Importantly, the enhancement of the convolution of the EXAFS maxima around k 6.2 Å⁻¹ (**Figure 3f**) appoints to partial Mo-N coordination, matching Mo-N features observed in MoN samples.^[54,55]

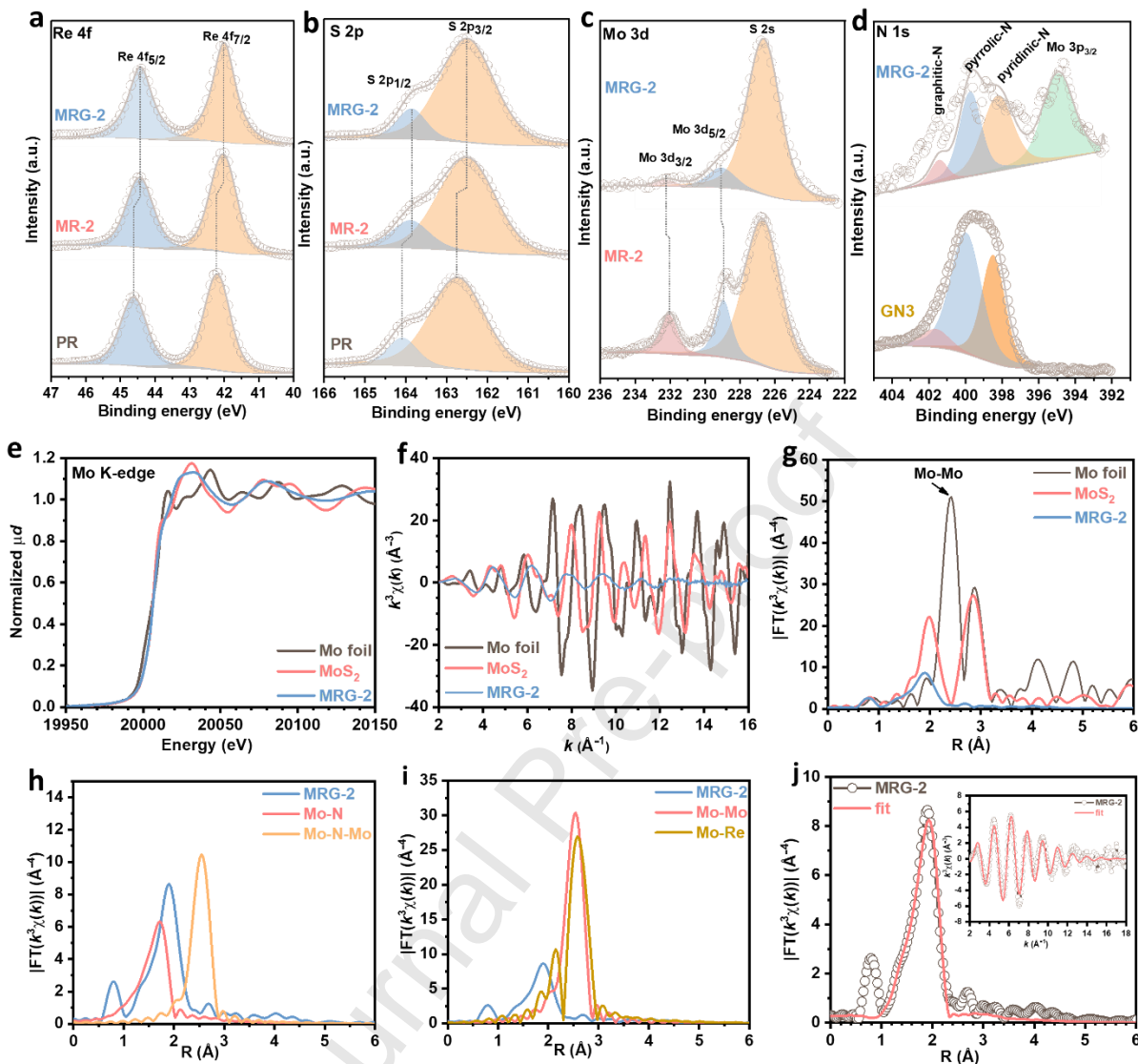


Figure 3. Comparative XPS spectra of PR, MR-2, MRG-2, and GN3, along with EXAFS measurements of MRG-2. High-resolution deconvoluted (a) Re 4f and (b) S 2p spectra of PR, MR-2, and MRG-2. (c) Mo 3d and (d) N 1s spectra of MR-2 and MRG-2. (e) Mo K-edge XANES spectra of Mo foil, commercial MoS₂, and MRG-2, along with (f) the corresponding k^3 -weighted EXAFS oscillations. (g) Fourier transforms obtained in the 3-16 Å⁻¹ k range using a Hanning window. (h, i) Calculated EXAFS FT for six-coordinated Mo-N and 12-coordinated Mo-Mo and Mo-Re bonds, with Debye-Waller factor fixed at 0.006 Å². (j) Mo K-edge EXAFS fit results for MRG-2, performed in the 3-16 Å⁻¹ k and 1-3 Å R ranges.

The Fourier-transformed (FT)-EXAFS spectrum of MRG-2 shows a dominant peak at around 2.0 Å, similar to the distances observed in MoS₂ (**Figure 3g**), corresponding to the primary Mo-S bonding (**Figure 3g and S9a**).^[56] Its asymmetry toward lower *R* is compatible with the coexistence of Mo-N coordination bonds (**Figure 3h**). It should be noted, however, that it is difficult, if not impossible, to distinguish between Mo-N, Mo-C, and Mo-O coordination bonds (**Figure 3h and S9b, c**). The *k*³-weighted FT-EXAFS spectrum of MRG-2 shows no second-shell contribution at ≈2.5 Å, indicating the absence of Mo-Mo or Mo-Re shells (Figure 3i) and confirming that Mo exists as single-atom sites coordinated to S and likely to a lighter element—probably N—within the 2D MRG-2 heterostructure. To further quantify the results, the EXAFS signals were fitted using the standard equation in the single scattering approximation,^[57] (**Table S4 and Figure 3j and S10**). Fits for Mo foil and MoS₂ references converged quickly with the experimental data (**Figure S10**).^[57] However, the EXAFS fit of the MRG-2 sample with the Mo-S shell did not yield sufficient agreement with experimental data. The inclusion of Mo-N bonds dramatically improved the fit agreement (**Figure 3j**), confirming the previously speculated presence of Mo-N coordination bonds. The MRG-2 hybrid system can be represented considering a 6-coordinated Mo atom bonded to S (91%) and N (9%) atoms.

Electrochemical Measurements

The electrochemical performance of the MRG-2 hybrid and its individual counterparts was evaluated in a three-electrode cell using 3 M KOH aqueous electrolyte within a potential range of -1.0 to -0.3 V *vs.* Ag/AgCl. The comparative cyclic voltammetry (CV) curves for PR, MR-2, GN3, and MRG-2 at a scan rate of 50 mV s⁻¹, showed the largest area under the CV curve

for MRG-2 (**Figure 4a**). The galvanostatic charge discharge (GCD) profiles recorded at a current density of 1 A g^{-1} also displayed the longest discharge time for the MRG-2 sample (**Figure 4b**). Evidently, MRG-2 exhibited the highest specific capacitance (C_{sp}) calculated from the GCD curve (228.6 F g^{-1}), followed by MR-2 (175 F g^{-1}), GN3 (161.5 F g^{-1}), and PR (122 F g^{-1}), all at 1 A g^{-1} (**Figure 4b**). The C_{sp} values in all cases were calculated from the GCD curves with the non-linear equation 1, provided in the SI. The C_{sp} decreased with increasing current density, typically attributed to insufficient time for electrolyte ions to penetrate into the pores of the electrode material (**Figure 4c**).^[58]

In view of the coordination bond observed between Mo in ReS_2 and N in GN3 from the EXAFS (**Figure 3**), we hypothesized that using a different type of graphene (such as rGO) without N atoms, would result in inferior properties. Thus, a control sample of 2D Mo- ReS_2 grown in-situ on rGO was synthesized under the same experimental conditions as MRG-2. This material (MR-rGO) exhibited a reduced area under the CV curve (**Figure S11a**) and a 20% decrease in C_{sp} compared to MRG-2 at 1 A g^{-1} (**Figure S11b**). The equivalent series resistance (R_s) values obtained from the Nyquist plots derived from electrochemical impedance spectroscopy (EIS, **Figure S11d**) indicated a lower R_s for MRG-2 (0.81Ω) compared to MR-rGO (0.99Ω). Furthermore, the steeper slope of the curve in the low-frequency region for MRG-2, compared to that of the MR-rGO hybrid, demonstrated a very effective charge-transport profile within the bulk of the electrode. These control experiments unveiled the significance of the Mo-N coordination bonds between the Mo in ReS_2 and N in GN3, leading to the significantly enhanced charge storage properties of MRG-2. In addition to the strong coupling between Mo- ReS_2 and GN3 through the Mo-N bond, other factors such as weak interlayer interactions in ReS_2 compared to MoS_2 and the improved electronic conductivity due to Mo p-doping are also crucial

for enhancing the charge storage properties. For example, the control MoS₂-GN3 hybrid sample achieved merely a 25.8% increase in C_{sp} over pristine MoS₂ (**Figure S12**), in contrast to the 87% increase in C_{sp} between the PR and MRG-2, clearly highlighting the importance of precisely controlling the presence of Mo only as single-atoms and at a certain content (**Figure S1**). Furthermore, the experimentally measured electronic conductivity of MR-2 was two-fold higher than that of PR (**Figure S13**). These observations are also supported by theoretical calculations^[44] of the band-structure changes upon Mo-doping of ReS₂ because: i) the Fermi level shifts downward into the valence band,^[44] with Mo filled d-orbitals populating the near-Fermi density of states^[42] and thus improving the interlayer coupling of the p-doped Mo-ReS₂ with the n-doped GN3 systems,^[34,36] ii) the band gap of ReS₂ decreases substantially upon Mo-doping, leading to an increase in conductivity.^[28] This highlights the importance of establishing covalent coordination bonds (Mo-N), which significantly enhance the charge storage performance of the MRG-2 hybrid, resulting in an 87% improved C_{sp} compared to PR.

The Nyquist plot of MRG-2 showed the lowest R_s of 0.81 Ω compared with PR (1.32 Ω), MR-2 (1.23 Ω), and GN3 (1.02 Ω). The low R_s value for the MRG-2 electrode material indicates faster electronic and ionic transport and reduced interfacial resistance in the electrode material, manifesting the strong coupling between GN3 and Mo_{0.22}Re_{0.78}S₂. Additionally, the absence of a semicircle in the high-frequency region demonstrates very low charge transfer resistance at the electrode/electrolyte interface. Meanwhile, the steeper slope for the MRG-2 hybrid compared to PR and MR-2 in the low frequency region suggests a more efficient ion diffusion process within the bulk of the electrode material. The EIS data, presented as a Bode impedance plot (**Figure S13d**), further indicate strong coupling between GN3 and Mo-ReS₂, thereby enhancing the conductivity of the MRG-2 heterostructure, as evidenced by (i) a downward shift of the high-

frequency $\text{Re}(Z)$ plateau in the Bode magnitude plot (Figure S13d, bottom panel); (ii) the higher phase angle for the MRG-2 across a broader intermediate frequency range, indicating minimal resistive losses; (iii) a shift of the peaks in the phase angle curve towards higher frequencies in the $\text{MRG-2} > \text{MR-2} > \text{PR}$ order (Figure S13d, upper panel). The reduction in electronic resistance within the bulk of the electrode was further corroborated by the enhanced electronic conductivity of the MRG-2 hybrid, measured by the four-probe method (**Figure S13**). The MRG-2 (6.1 S m^{-1}) exhibited more than four-fold and two-fold higher electrical conductivity than PR (1.5 S m^{-1}) and MR-2 (3.01 S m^{-1}), respectively (**Figure S13**).

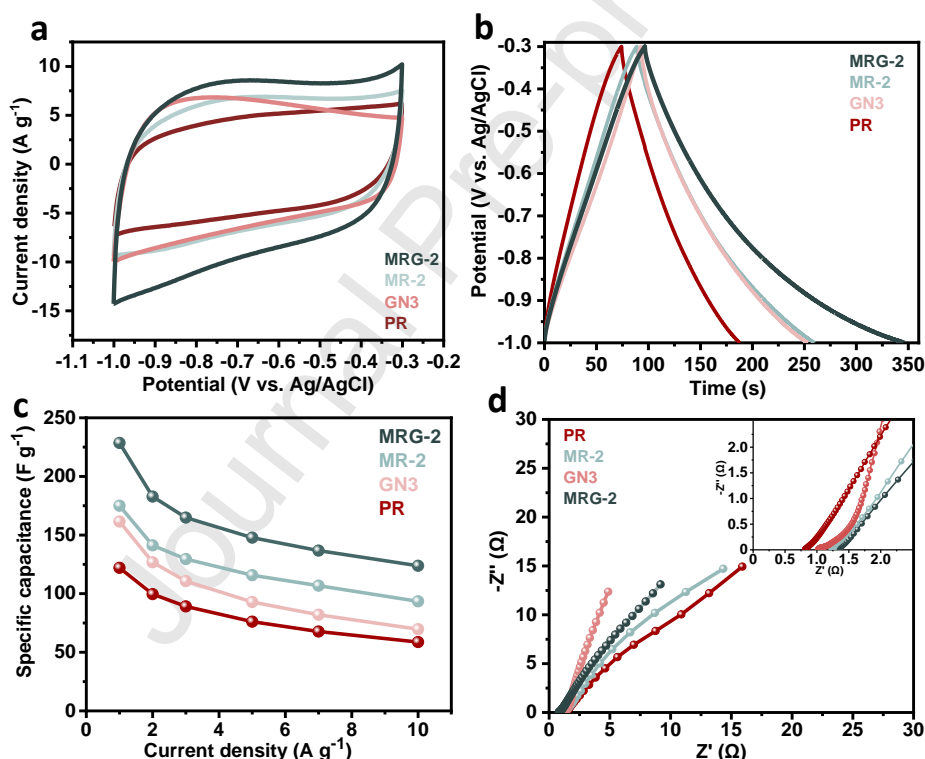


Figure 4. Electrochemical measurements of PR, MR-2, GN3, and MRG-2 in an open cell, three electrode configuration using 3 M KOH (a) Comparative CV curves of PR, MR-2, GN3, and MRG-2 at a scan rate of 50 mV s^{-1} . (b) GCD curves of PR, MR-2, GN3, and MRG-2 at a current density of 1 A g^{-1} . (c) Specific capacitance as a function of current density for PR, MR-2, GN3, and MRG-2. (d) Nyquist plots of PR, MR-2, GN3, and MRG-2 samples. The inset is a zoom in the high frequency region from where the ESR is determined.

The CV curves of the MRG-2 hybrid at different scan rates displayed a nearly rectangular shape (**Figure 5a**), which was well-maintained even at higher scan rates, indicating good rate capability. Furthermore, the nearly symmetrical triangular GCD profiles of MRG-2 at different current densities suggest capacitive behavior and good rate capability (**Figure 5b**). To gain insight into the operational mechanism of the MRG-2 electrode material, electrochemical kinetics were evaluated from the CV curves recorded at different scan rates (**Figure 5a**), using a power law analysis. The b -value was calculated from the slope of the log-log plot of current (i) versus scan rate (v) at different potentials, according to the equation $i_p = av^b$.^[59] The MRG-2 sample demonstrated the cathodic potential sweep b -values of 0.71 and 0.67 at -0.8 V and -0.4 V potentials, respectively (**Figure S14a, b**). This suggests that the current response involves both surface-controlled (capacitive) and diffusion-controlled processes. For the anodic potential sweep, the b -values were 1.05 and 0.95 at -0.8 V and -0.4 V, respectively (**Figure S14a, c**), suggesting a dominant capacitive contribution.^[24,60]

The relative contributions of the diffusion- and surface-controlled processes were quantified using the Dunn equation ($i = k_1v + k_2v^{1/2}$).^[24,59] The k_1v and $k_2v^{1/2}$ represent the surface-controlled and diffusion-limited current contributions, respectively, to the total current; v is the potential sweep rate, and k_1 and k_2 are constants independent from the potential sweep-rate. The shaded portion of the CV curve of MRG-2 at 20 mV s⁻¹ represents the contribution from diffusion-controlled processes (**Figure 5c**). The capacitive contribution increased from 33% at 5 mV s⁻¹ to 67% at 50 mV s⁻¹, and levelled off at 72% at 100 mV s⁻¹ (**Figure 5d**). Furthermore, the dQ/dV plots for MRG-2, derived from the GCD data in a three-electrode cell at different current densities, exhibit a rectangular shape with only a slight decrease in area at higher current

densities (**Figure S15**). This behavior further confirms that the charge storage is predominantly governed by a surface-controlled (capacitive) process.

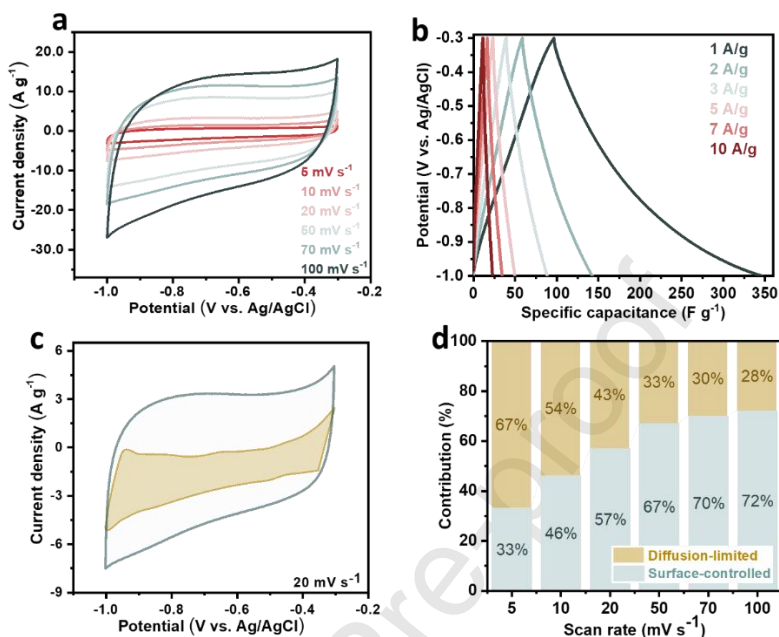


Figure 5. (a) CV curves of MRG-2 at different scan rates. (b) GCD profiles of MRG-2 at different current densities. (c) CV curve of MRG-2 showing diffusion-controlled contribution to total current (shaded area) at a scan rate of 20 mV s⁻¹. (d) diffusion- and surface-controlled charge storage contribution of MRG-2 at different scan rates.

The practical applicability of the MRG-2 heterostructure in terms of energy and power density was evaluated by assembling an asymmetric supercapacitor full cell (ASC) device using 3 M KOH aqueous electrolyte. The ASC device was assembled by employing MRG-2 as a negative (-1.0 V to -0.3 V) and NiCo₂S₄/graphene (NCSG) as a positive (-0.3 V to 0.5 V) electrode, resulting in a broader potential window up to 1.5 V, with a mass loading of 1 mg cm⁻². NCSG was selected for its well-documented performance as a positive electrode.^[7] The total mass density considering the thickness of both electrodes was estimated to be 1.88 g cm⁻³, which is used to calculate the volumetric characteristics of the electrodes for the full cell. The synthesis and characterization of NCSG are provided in the SI (**Figures S16 and S17**). The charges

between the negative (MRG-2) and positive (NCSG) electrodes were balanced by recording their CV responses in their respective potential windows at 10 mV s^{-1} (**Figure S18**). Accordingly, the mass ratio was evaluated to be $m_+ = 0.27 \text{ m.}$ (**equation 2, SI**). The CV of the MRG-2//NCSG device, recorded at scan rates ranging from 5 to 100 mV s^{-1} , showed that the overall capacitance is a combination of pseudo- and electric double-layer capacitance (**Figure 6a**). The GCD profiles at different current densities showed almost symmetrical curves, indicating good electrochemical reversibility of the ASC device. Additionally, the small IR drop of 0.037 V at 5 A g^{-1} (**Figure 6b**), demonstrates low resistivity of the electrodes and efficient ion transport at the electrode/electrolyte interface. The ASC device achieved a high gravimetric capacitance (C_g) of 187.5 F g^{-1} at 0.5 A g^{-1} , retaining 116 F g^{-1} at 10 A g^{-1} (C_g was calculated according to non-linear **equation 3, SI**), demonstrating an excellent rate performance of 62.0%. Even at a very high current density of 20 A g^{-1} , the device maintained a C_g of 99.9 F g^{-1} (**Figure 6c**). The excellent rate capability of the MRG-2//NCSG ASC device is evident when compared with previously reported full-cell ASC devices based on similar systems.^[8,61] For example, $\text{NiMo}_3\text{S}_4/\text{BP}/\text{NiCo}_2\text{S}_4/\text{Ti}_3\text{C}_2\text{S}_4$ retained 59.5% of its initial capacitance at its maximum reported current density of 1 A g^{-1} ,^[8] and P-mediated $\text{MoS}_2/\text{MnO}_2$ retained 34% at 16 A g^{-1} ,^[61] which is lower compared to the MRG-2//NCSG ASC device at a higher current density of 20 A g^{-1} (53%) (**Figure 6c**).

The Ragone plot (energy density vs. power density) is crucial for evaluating the performance of SC devices, with the herein MRG-2//NCSG ASC delivering a high gravimetric energy density (E_g) of 58.6 Wh kg^{-1} at a power density (P_g) of 0.5 kW kg^{-1} , retaining 25.4 Wh kg^{-1} even at 20.0 kW kg^{-1} (**Figure 6d**). The volumetric characteristics of SC are critical for advancing portable energy storage solutions.^[1,2] The MRG-2//NCSG ASC device delivered an extremely high volumetric energy density (E_v) of $110.5 \text{ mWh cm}^{-3}$ at a power density (P_v) of

0.94 W cm⁻³, retaining as high as 47.9 mWh cm⁻³ at 37.7 Wcm⁻³. Interestingly, the areal energy density (E_a) is also particularly high, reaching 54.3 μWh cm⁻² at a power density (P_a) of 1.0 mW cm⁻². Notably, the gravimetric, volumetric, and areal performance of the MRG-2//NCSG ASC device not only outperformed the previously reported ReS₂-based systems, but also other top-rated advanced electrode materials, including 2D TMDs and transition metal sulfide systems (Figure 6e-g, Tables S1 and S2). The detailed comparisons also revealed that the gravimetric and volumetric performances of MRG-2//NCSG ASC device operating in a low-cost aqueous electrolyte outperform devices operating even under a wide potential window using organic and water-in-salt electrolytes (Tables S1 and S2).

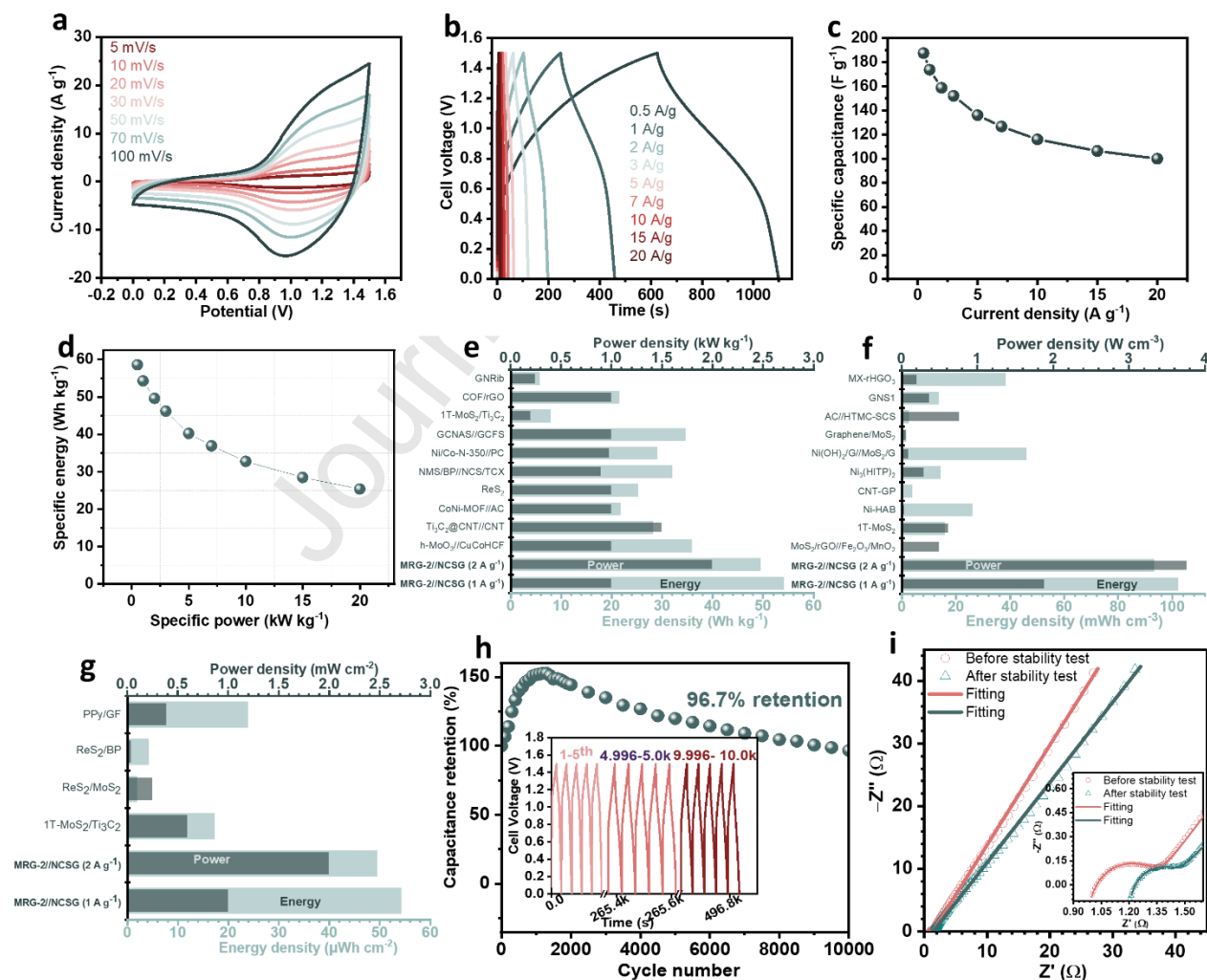


Figure 6. Electrochemical studies of MRG-2//NCSG ASC device: (a) CV curves at variable scan rates. (b) GCD profiles at different current densities. (c) Rate performance. (d) Ragone plot. (e-g) Comparison of the gravimetric, volumetric, and areal energy and power density output obtained with the MRG-2//NCSG ASC device with respect to advanced electrode materials selected from the literature. More details are given in Tables S1 and S2. (h) Cycling stability of MRG-2//NCSG ASC device at a constant current density of 8 A g^{-1} . (i) Nyquist plots of MRG-2//NCSG ASC device before and after cycling stability test and magnified high-frequency region (inset-i). (panels e-g, explanation of abbreviations of materials *h*-MoO₃//CuCoHCF: asymmetric pseudocapacitor device based on hexagonal molybdenum oxide/Prussian blue analogue,^[6] Ti₃C₂@CNT//CNT: ASC based on MXene-knotted carbon nanotube//carbon nanotube,^[9] CoNi-MOF//AC: asymmetric SC based on oriented cobalt nickel-MOF on carbon fiber paper//activated carbon (Adv. Energy Mater.^[11]), ReS₂: rhenium disulfide,^[31] NMS/BP//NCS/TCX: asymmetric SC based on nickel molybdenum sulfide/black phosphorous//nickel cobalt sulfide/MXene,^[8] Ni/Co-N-350//PC: asymmetric SC based on Ni-doped cobalt-cobalt nitride//porous carbon,^[62] GCNAS//GCFS: asymmetric SC based on graphene/cobalt nickel aluminum sulfide//graphene/cobalt iron sulfide,^[38] 1T MoS₂/Ti₃C₂: symmetric SC based on molybdenum disulfide/MXene,^[24] COF/rGO: symmetric SC device based on covalent organic framework/reduced graphene oxide,^[10] GNRib: MOF derived Graphene nanoribbons,^[63] MoS₂/rGO//Fe₂O₃/MnO₂: Molybdenum disulfide/reduced graphene oxide//iron oxide/manganese oxide core shell nanorods based asymmetric SC,^[22] 1T MoS₂: 1T molybdenum disulfide,^[5] Ni-HAB: Nickel-hexaaminobenzene MOF,^[64] CNT-GP: carbon nanotubes/graphene petals,^[4] Ni₃(HITP)₂: Nickel-Hexaimino triphenylene,^[39] Ni(OH)₂/G//MoS₂/G: asymmetric SC based on nickel hydroxide/graphene//molybdenum disulfide/graphene,^[23] Graphene/MoS₂: compact graphene/molybdenum disulfide,^[65] AC//HTMC-SCS: activated carbon//hierarchical transition metal (Cu-Ni) chalcogenide shell-core-shell,^[66] GNS1: graphene nanospheres,^[67] MX-rHGO₃: MXene/holey graphene,^[68] ReS₂/MoS₂: rhenium disulfide/molybdenum disulfide,^[33] ReS₂/BP: rhenium disulfide coupled with black phosphorus,^[69] PPy/GF: polypyrrole coated graphene foam.^[70]

Another important parameter for evaluating the performance of an ASC device is its cycling stability. For the MRG-2//NCSG ASC device, the capacitance was initially increased by up to 150 % due to the electrochemical activation of the electrode material.^[71] The activation of the electrode material during the initial cycles was confirmed by the increased area under the peaks in the differential capacity plot (**Figure S19**), which is likely attributed to the more effective participation of active material in the Faradaic redox processes.^[72] This activation is usually connected to the progressively deeper and more effective penetration of the electrolyte ions into the pores of the material during charging/discharging, enhancing charge storage.^[71] The device retained 96.7% of its capacitance even after 10,000 charge-discharge cycles at 8 A g^{-1} (**Figure 6h**). The cycling stability exceeds that of current state-of-the-art systems (**Tables S1 and S2**). For instance, $\text{NiMo}_3\text{S}_4/\text{BP}/\text{NiCo}_2\text{S}_4/\text{Ti}_3\text{C}_2\text{T}_x$ -based ASC device retained 86% of its initial capacitance after 5,000 cycles at 10 A g^{-1} ,^[8] $h\text{-MoO}_3/\text{Cu}_{0.82}\text{Co}_{0.18}\text{HCF}$ maintained 83% of initial capacitance after 10,000 cycles at 10 A g^{-1} ,^[6] and a $(\text{Ni},\text{Co})_3\text{S}_4/\text{graphene}$ ASC retained 85% after 10000 cycles,^[7] and many other systems mentioned in **Tables S1 and S2**.

The EIS measurements of the full cell at open circuit potential were conducted before and after the cycling stability test (**Figure 6i and inset**) and fitted using a modified Randles circuit (**Figure S20 and Table S5**). Before cycling, the Nyquist plot revealed a charge transfer resistance (R_{ct}) of 0.42Ω (**Table S5**), indicating fast electrochemical kinetics (**Figure 6i and inset**). The Warburg region displayed a slope greater than 45° , suggesting the presence of diffusion restrictions (**Figure 6i**). After the stability test, the R_{ct} substantially decreased to 0.25Ω (**Table S5**), demonstrating excellent electrochemical stability of the electrode. Additionally, the Warburg slope shifted to $\sim 45^\circ$ (**Figure 6i**), indicating improved ion diffusion due to material activation during cycling, as also suggested by the cycling stability test (**Figure 6h**).^[71]

Overall, the key characteristics of the MRG-2 electrode material that contribute to the excellent electrochemical performance of the MRG-2//NCSG ASC device can be ascribed to the following points: i) Mo single-atom doping in the 1T' ReS₂ modifies the electronic structure by lowering the band gap and enhances activity of the in-plane S atoms. ii) seamless hybridization of Mo-ReS₂ with 2D conductive GN3 leads to a more open architecture with improved porosity and surface area, as indicated by SAXS and BET measurements, iii) strong interfacial coupling between Mo atoms in Mo-ReS₂ and N in GN3 via Mo-N coordination bonding as evidenced by EXAFS analysis, leads to enhanced electrical conductivity and fast charge transport kinetics, as supported by four-probe electrical measurements and EIS, respectively. These advancements have transformed ReS₂ from a previously underperforming TMD into one of the top-tier SC electrode materials. Interfacial engineering through single-atom incorporation has proven invaluable for tuning crucial properties, including conductivity, charge transport, and surface activity through the combined modulation of the electronic and the chemical structure at the phase boundaries of thin 2D materials. This previously untapped strategy opens new opportunities for more efficient energy storage solutions.

Conclusions

This work introduces a strategy to effectively modulate the electronic structure of 2D 1T' ReS₂ through controlled incorporation of Mo at the atomic scale, followed by strong interfacial coupling with a conductive superdoped graphene derivative, produced via fluorographene. The formation of the 1T' ReS₂ phase and the electronic modifications induced by Mo doping were confirmed by XRD, Raman, and XPS analyses. EXAFS studies confirm strong interfacial

coupling between Mo atoms in Mo-ReS₂ and N in GN3 through Mo-N coordination bond. The resulting 2D Mo-ReS₂@GN3 (MRG-2) heterostructure demonstrates significantly improved electrical conductivity, charge transport kinetics, and porosity, as confirmed by four-probe conductivity, EIS and SAXS measurements, respectively. Control experiments with materials synthesized without Mo or with graphene lacking nitrogen dopants highlight the crucial role of Mo single-atom doping and Mo-N bonding in optimizing electrochemical performance. Leveraging these synergistic effects, the MRG-2 heterostructure delivers superior electrochemical performance compared to its individual components measured in 3 M KOH. Furthermore, an asymmetric full cell device, employing 2D MRG-2 as negative electrode and NCSG as positive electrode, exhibits outstanding charge storage properties, rate capability, and long cyclability. Notably, the MRG-2//NCSG ASC device achieves exceptional simultaneous gravimetric (54.3 Wh kg⁻¹ at 1.0 kW kg⁻¹), volumetric (110.5 mWh cm⁻³ at 0.94 W cm⁻³), and areal (54.3 μWh cm⁻² at 1.0 mW cm⁻²) energy densities, underscoring its potential for high-performance, compact energy storage solutions. By introducing a previously unutilized function of single-atom interfacial engineering in TMD-based heterostructures, this work provides a transformative approach to overcoming fundamental limitations in charge storage materials, where the communication between phase boundaries plays a crucial role. The findings pave the way for a new design paradigm in supercapacitor electrodes, with broad implications for next-generation energy storage technologies.

Acknowledgements

M. Khandelwal acknowledges the support from the European Union's Horizon 2020 research and innovation programme under the Marie Skłodowska-Curie grant agreement No 101180679.

Funded by the European Union. Views and opinions expressed are however those of the author(s) only and do not necessarily reflect those of the European Union or European Commission. Neither the European Union nor the granting authority can be held responsible for them. I. Obraztsov and A. Bakandritsos acknowledge support from the Czech Science Foundation (grant no. 22-27973K; project GRAPHMAX). We acknowledge support from the ERDF/ESF project TECHSCALE (No. CZ.02.01.01/00/22_008/0004587) and support from the European Union under the project REFRESH - Research Excellence for Region Sustainability and High-tech Industries (CZ.10.03.01/00/22_003/0000048) via the Operational Programme Just Transition from the Ministry of the Environment of the Czech Republic. We thank Dr. Viktorie Víchová for XRD and BET, Dr. Eirini Ioannou for SEM, Jana Straska for TEM, Ondrej Tomanec for HR-TEM, and Emil Remeslnicek for TGA.

Author Contributions

M.K.: Methodology, experimental, analysis, writing-original draft, investigation, visualization, funding acquisition; I.O.: Methodology, experimental, analysis, investigation; A.C.P. and S.S.: Experimental, data analysis and discussion; G.E., O.U., L.S., and G.P.: EXAFS, SAXS, and WAXS measurements and analysis; R.Z.: supervision, funding acquisition, review & editing; A.B.: Supervision, funding acquisition, visualization, writing original draft, review, and editing.

Conflict of Interest

The authors declare no conflict of interest. They have no known competing financial interests or personal relationships that could have appeared to influence the work reported in this paper.

Data Availability Statement

The data accompanying this work are available in this link as a power point file in the form of editable origin graphs. If the work is accepted, all data will be published in Zenodo in the form of xy data files, with the statement “The data that support the findings of this study are openly available in Zenodo at [DOI].”

References

- [1] S. Pohlmann, *Nat. Commun.* **2022**, *13*, 1538.
- [2] C. Zhang, W. Lv, Y. Tao, Q.-H. Yang, *Energy Environ. Sci.* **2015**, *8*, 1390.
- [3] W. Zhang, C. Xu, C. Ma, G. Li, Y. Wang, K. Zhang, F. Li, C. Liu, H.-M. Cheng, Y. Du, N. Tang, W. Ren, *Adv. Mater.* **2017**, *29*, 1701677.
- [4] G. Xiong, P. He, Z. Lyu, T. Chen, B. Huang, L. Chen, T. S. Fisher, *Nat. Commun.* **2018**, *9*, 790.
- [5] M. Acerce, D. Voiry, M. Chhowalla, *Nat. Nanotechnol.* **2015**, *10*, 313.
- [6] T. Xu, Z. Xu, T. Yao, M. Zhang, D. Chen, X. Zhang, L. Shen, *Nat. Commun.* **2023**, *14*, 8360.
- [7] J. Yang, C. Yu, X. Fan, S. Liang, S. Li, H. Huang, Z. Ling, C. Hao, J. Qiu, *Energy Environ. Sci.* **2016**, *9*, 1299.
- [8] M. Pathak, P. Mane, B. Chakraborty, J. S. Cho, S. M. Jeong, C. S. Rout, *Small* **2024**, *20*, 2310120.
- [9] X. Gao, X. Du, T. S. Mathis, M. Zhang, X. Wang, J. Shui, Y. Gogotsi, M. Xu, *Nat. Commun.* **2020**, *11*, 6160.
- [10] C. Li, J. Yang, P. Pachfule, S. Li, M.-Y. Ye, J. Schmidt, A. Thomas, *Nat. Commun.* **2020**, *11*, 4712.
- [11] T. Deng, Y. Lu, W. Zhang, M. Sui, X. Shi, D. Wang, W. Zheng, *Adv. Energy Mater.* **2018**, *8*, 1702294.
- [12] W. Guo, C. Dun, C. Yu, X. Song, F. Yang, W. Kuang, Y. Xie, S. Li, Z. Wang, J. Yu, G. Fu, J. Guo, M. A. Marcus, J. J. Urban, Q. Zhang, J. Qiu, *Nat. Commun.* **2022**, *13*, 1409.
- [13] J. Li, Z. Guo, W. Zhang, J. Guo, K. Qu, W. Cai, *Green Energy Environ.* **2023**, *8*, 559.
- [14] J. Shi, H. He, Y. Guo, F. Ji, J. Li, Y. Zhang, C. Deng, L. Fan, W. Cai, *J. Energy Chem.* **2023**, *85*, 76.
- [15] S. Zhou, J. Wang, J. Li, L. Fan, Z. Liu, J. Shi, W. Cai, *Appl. Catal. B Environ.* **2023**, *332*, 122749.
- [16] H.-B. Zhang, Y. Meng, L. Fang, F. Yang, S. Zhu, T. Li, X. Yu, J. Rong, W. Chen, D. Su, Y. Mei, P.-X. Hou, C. Liu, M. Shao, J.-C. Li, *Energy Environ. Sci.* **2024**, *17*, 9375.
- [17] L. Lin, W. Lei, S. Zhang, Y. Liu, G. G. Wallace, J. Chen, *Energy Storage Mater.* **2019**, *19*, 408.
- [18] C. Tan, H. Zhang, *Chem. Soc. Rev.* **2015**, *44*, 2713.
- [19] Y. Xue, Q. Zhang, W. Wang, H. Cao, Q. Yang, L. Fu, *Adv. Energy Mater.* **2017**, *7*, 1602684.

- [20] W. Liu, M. Zhang, M. Li, B. Li, W. Zhang, G. Li, M. Xiao, J. Zhu, A. Yu, Z. Chen, *Adv. Energy Mater.* **2020**, *10*, 1903724.
- [21] S. Lee, J. Hwang, D. Kim, H. Ahn, *Chem. Eng. J.* **2021**, *419*, 129701.
- [22] D. Sarkar, D. Das, S. Das, A. Kumar, S. Patil, K. K. Nanda, D. D. Sarma, A. Shukla, *ACS Energy Lett.* **2019**, *4*, 1602.
- [23] Q. Ke, X. Zhang, W. Zang, A. M. Elshahawy, Y. Hu, Q. He, S. J. Pennycook, Y. Cai, J. Wang, *Small* **2019**, *15*, 1900131.
- [24] X. Wang, H. Li, H. Li, S. Lin, W. Ding, X. Zhu, Z. Sheng, H. Wang, X. Zhu, Y. Sun, *Adv. Funct. Mater.* **2020**, *30*, 0190302.
- [25] X. Yin, W. Zheng, H. Tang, P. Zhang, Z. Sun, *Nanoscale* **2023**, *15*, 10437.
- [26] S. Tongay, H. Sahin, C. Ko, A. Luce, W. Fan, K. Liu, J. Zhou, Y.-S. Huang, C.-H. Ho, J. Yan, D. F. Ogletree, S. Aloni, J. Ji, S. Li, J. Li, F. M. Peeters, J. Wu, *Nat. Commun.* **2014**, *5*, 3252.
- [27] Q. Zhang, L. Fu, *Chem* **2019**, *5*, 505.
- [28] H. Li, Y. Wang, G. Liu, L. Wei, D. Wang, *J. Mol. Model.* **2022**, *28*, 93.
- [29] M. Rahman, K. Davey, S.-Z. Qiao, *Adv. Funct. Mater.* **2017**, *27*, 1606129.
- [30] J. Pan, R. Wang, X. Xu, J. Hu, L. Ma, *Nanoscale* **2019**, *11*, 10402.
- [31] P. Pazhamalai, K. Krishnamoorthy, V. K. Mariappan, A. Sathyaseelan, S.-J. Kim, *Mater. Chem. Front.* **2020**, *4*, 3290.
- [32] Z. Lai, S. Rong, S. Huang, M. Qin, J. Huang, X. Zhang, Z. Zhang, J. Liu, *Surf. Interfaces* **2023**, *42*, 103494.
- [33] S. Manoj, H. K. Sadhanala, I. Perelshtein, A. Gedanken, *ACS Appl. Mater. Interfaces* **2022**, *14*, 18570.
- [34] J. Ge, J. Meng, L. Zhang, J. Qin, G. Yang, Y. Wu, H. Zhu, Y. Huang, E. Debroye, H. Dong, J. Ren, P. He, J. Hofkens, F. Lai, T. Liu, *Small* *n/a*, 2312019.
- [35] K. Li, X. Wang, S. Li, P. Urbankowski, J. Li, Y. Xu, Y. Gogotsi, *Small* **2020**, *16*, 1906851.
- [36] Y. Jian, X. Song, X. Wang, C. Zhu, T. Guo, S. Zhang, X. Chen, X. Chen, H. Zeng, *ACS Appl. Electron. Mater.* **2022**, *4*, 6013.
- [37] V. Šedajová, A. Bakandritsos, P. Błoński, M. Medved', R. Langer, D. Zaoralová, J. Ugolotti, J. Džibelová, P. Jakubec, V. Kupka, M. Otyepka, *Energy Environ. Sci.* **2022**, *15*, 740.
- [38] W. Liu, H. Niu, J. Yang, K. Cheng, K. Ye, K. Zhu, G. Wang, D. Cao, J. Yan, *Chem. Mater.* **2018**, *30*, 1055.
- [39] D. Sheberla, J. C. Bachman, J. S. Elias, C.-J. Sun, Y. Shao-Horn, M. Dincă, *Nat. Mater.* **2017**, *16*, 220.
- [40] B. Chen, H. Li, H. Liu, X. Wang, F. Xie, Y. Deng, W. Hu, K. Davey, N. Zhao, S.-Z. Qiao, *Adv. Energy Mater.* **2019**, *9*, 1901146.
- [41] J. He, A. Bhargav, H. Yaghoobnejad Asl, Y. Chen, A. Manthiram, *Adv. Energy Mater.* **2020**, *10*, 2001017.
- [42] J. Wang, J. He, G. Omololu Odunmbaku, S. Zhao, Q. Gou, G. Han, C. Xu, T. Frauenheim, M. Li, *Chem. Eng. J.* **2021**, *414*, 128811.
- [43] Q. Sun, B. Zhang, L. Diao, B. Chen, K. Song, L. Ma, F. He, *J. Mater. Chem. A* **2020**, *8*, 11607.
- [44] J.-K. Qin, W.-Z. Shao, C.-Y. Xu, Y. Li, D.-D. Ren, X.-G. Song, L. Zhen, *ACS Appl. Mater. Interfaces* **2017**, *9*, 15583.
- [45] H. T. T. Nguyen, L. A. Adofo, S.-H. Yang, H.-J. Kim, S. H. Choi, B. Kirubasankar, B. W. Cho, A. Ben-Smith, J. Kang, Y.-M. Kim, S. M. Kim, Y.-K. Han, K. K. Kim, *Adv. Funct. Mater.* **2023**, *33*, 2209572.

- [46] C. T. Cao, S.-W. Kim, H. J. Kim, R. Purbia, S. H. Kim, D. Kim, K. J. Choi, H. Park, J. M. Baik, *Nano Energy* **2022**, 96, 107117.
- [47] D. Gao, W. Zhong, X. Zhang, P. Wang, H. Yu, *Small* **2024**, 20, 2309123.
- [48] Y. Lv, W. Lei, S. Liu, W.-H. Zhang, *Adv. Electron. Mater.* **2019**, 5, 1800830.
- [49] J. Suh, T.-E. Park, D.-Y. Lin, D. Fu, J. Park, H. J. Jung, Y. Chen, C. Ko, C. Jang, Y. Sun, R. Sinclair, J. Chang, S. Tongay, J. Wu, *Nano Lett.* **2014**, 14, 6976.
- [50] X. Liu, J. Wang, Y. Lin, J. Zhou, Q. Liu, W. Yu, Y. Cai, X. Li, V. D. Botcha, T. Rao, S. Huang, *ACS Omega* **2022**, 7, 48301.
- [51] J. Xu, W. Zhong, X. Zhang, X. Wang, X. Hong, H. Yu, *Small* **2023**, 19, 2303960.
- [52] P. Ou, X. Zhou, F. Meng, C. Chen, Y. Chen, J. Song, *Nanoscale* **2019**, 11, 13600.
- [53] L. Huo, X. Han, L. Zhang, B. Liu, R. Gao, B. Cao, W.-W. Wang, C.-J. Jia, K. Liu, J. Liu, J. Zhang, *Appl. Catal. B Environ.* **2021**, 294, 120254.
- [54] Z. Jin, M. Yang, Y. Dong, X. Ma, Y. Wang, J. Wu, J. Fan, D. Wang, R. Xi, X. Zhao, T. Xu, J. Zhao, L. Zhang, D. J. Singh, W. Zheng, X. Cui, *Nano-Micro Lett.* **2023**, 16, 4.
- [55] W. Chen, J. Pei, C.-T. He, J. Wan, H. Ren, Y. Zhu, Y. Wang, J. Dong, S. Tian, W.-C. Cheong, S. Lu, L. Zheng, X. Zheng, W. Yan, Z. Zhuang, C. Chen, Q. Peng, D. Wang, Y. Li, *Angew. Chem. Int. Ed.* **2017**, 56, 16086.
- [56] Y. Ma, D. Leng, X. Zhang, J. Fu, C. Pi, Y. Zheng, B. Gao, X. Li, N. Li, P. K. Chu, Y. Luo, K. Huo, *Small* **2022**, 18, 2203173.
- [57] S. Caramazza, C. Marini, L. Simonelli, P. Dore, P. Postorino, *J. Phys. Condens. Matter* **2016**, 28, 325401.
- [58] M. Khandelwal, S. H. Hur, J. S. Chung, *Chem. Eng. J.* **2019**, 363, 120.
- [59] M. Forghani, S. W. Donne, *J. Electrochem. Soc.* **2018**, 165, A664.
- [60] Q. Tao, M. Dahlqvist, J. Lu, S. Kota, R. Meshkian, J. Halim, J. Palisaitis, L. Hultman, M. W. Barsoum, P. O. Å. Persson, J. Rosen, *Nat. Commun.* **2017**, 8, 14949.
- [61] S. Liu, Y. Yin, M. Wu, K. S. Hui, K. N. Hui, C.-Y. Ouyang, S. C. Jun, *Small* **2019**, 15, 1803984.
- [62] X. Liu, W. Zang, C. Guan, L. Zhang, Y. Qian, A. M. Elshahawy, D. Zhao, S. J. Pennycook, J. Wang, *ACS Energy Lett.* **2018**, 3, 2462.
- [63] P. Pachfule, D. Shinde, M. Majumder, Q. Xu, *Nat. Chem.* **2016**, 8, 718.
- [64] D. Feng, T. Lei, M. R. Lukatskaya, J. Park, Z. Huang, M. Lee, L. Shaw, S. Chen, A. A. Yakovenko, A. Kulkarni, J. Xiao, K. Fredrickson, J. B. Tok, X. Zou, Y. Cui, Z. Bao, *Nat. Energy* **2018**, 3, 30.
- [65] N. Li, T. Lv, Y. Yao, H. Li, K. Liu, T. Chen, *J. Mater. Chem. A* **2017**, 5, 3267.
- [66] Y.-W. Lee, B.-S. Kim, J. Hong, H. Choi, H.-S. Jang, B. Hou, S. Pak, J. Lee, S.-H. Lee, S. M. Morris, D. Whang, J.-P. Hong, H. S. Shin, S. Cha, J. I. Sohn, J. M. Kim, *Nano Energy* **2017**, 37, 15.
- [67] Z. Yan, Z. Gao, Z. Zhang, C. Dai, W. Wei, P. K. Shen, *Small* **2021**, 17, 2007915.
- [68] Z. Fan, Y. Wang, Z. Xie, D. Wang, Y. Yuan, H. Kang, B. Su, Z. Cheng, Y. Liu, *Adv. Sci.* **2018**, 5, 1800750.
- [69] J. Ge, J. Meng, L. Zhang, J. Qin, G. Yang, Y. Wu, H. Zhu, Y. Huang, E. Debroye, H. Dong, J. Ren, P. He, J. Hofkens, F. Lai, T. Liu, *Small* **2024**, 20, 2312019.
- [70] H. Park, J. W. Kim, S. Y. Hong, G. Lee, D. S. Kim, J. hyun Oh, S. W. Jin, Y. R. Jeong, S. Y. Oh, J. Y. Yun, J. S. Ha, *Adv. Funct. Mater.* **2018**, 28, 1707013.
- [71] S. V. Talande, A. Bakandritsos, L. Zdražil, P. Jakubec, E. Mohammadi, O. Tomanec, M. Otyepka, V. Presser, R. Zbořil, J. Tuček, *J. Mater. Chem. A* **2020**, 8, 25716.
- [72] R. Xie, H. Huang, X. Qi, G. Wei, *J. Energy Storage* **2021**, 35, 102258.

Journal Pre-proof

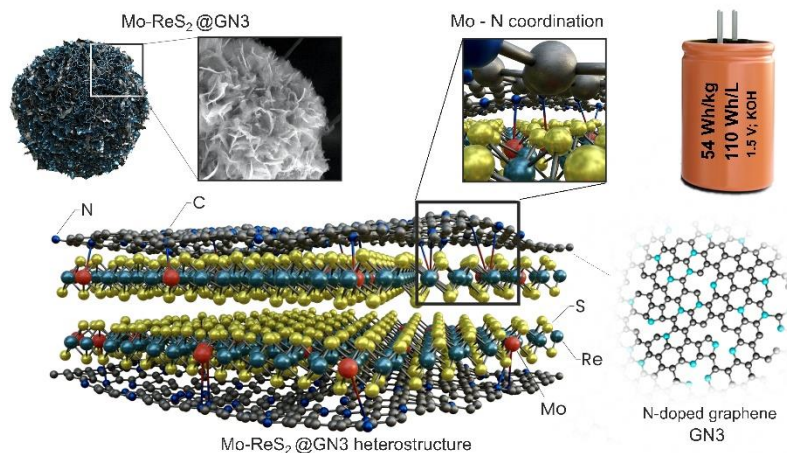
Declaration of interests

☒ The authors declare that they have no known competing financial interests or personal relationships that could have appeared to influence the work reported in this paper.

☐ The authors declare the following financial interests/personal relationships which may be considered as potential competing interests:

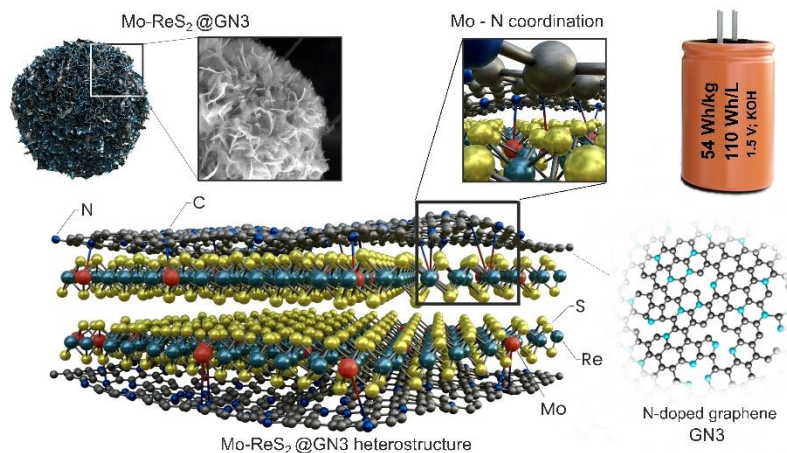
Journal Pre-proof

Table of Contents



This work demonstrates the modulation of 2D 1T' ReS₂ structure through Mo single-atom engineering, followed by strong interfacial coupling with GN3, improving charge transport kinetics, porosity and charge storage. The assembled asymmetric SC device achieved exceptional gravimetric (54.3 Wh kg⁻¹), volumetric (110.5 mWh cm⁻³), and areal (54.3 μWh cm⁻²) energy densities unlocking the potential of ReS₂ in energy storage.

Table of Contents



Highlights

- The electronic structure of 2D 1T' ReS₂ was modulated through Mo single-atom engineering, followed by strong interfacial coupling with N-doped graphene (GN3).
- The 2D Mo-ReS₂@GN3 heterostructure exhibits improved charge transport kinetics, porosity, and charge storage.
- The assembled asymmetric SC device achieved exceptional gravimetric (54.3 Wh kg⁻¹), volumetric (110.5 mWh cm⁻³), and areal (54.3 μWh cm⁻²) energy densities unlocking the potential of ReS₂ in energy storage.